Roles for L_o microdomains and ESCRT in ER stress-induced lipid droplet microautophagy in budding yeast

Pin-Chao Liao†, Enrique J. Garcia†, Gary Tan, Catherine A. Tsang, and Liza A. Pon*
Department of Pathology and Cell Biology, Columbia University, New York, NY 10032

ABSTRACT **Microlipophagy (μLP), degradation of lipid droplets (LDs) by microautophagy, occurs by autophagosome-independent direct uptake of LDs at lysosomes/vacuoles in response to nutrient limitations and ER stressors in *Saccharomyces cerevisiae*. In nutrient-limited yeast, liquid-ordered (L_o) microdomains, sterol-rich raftlike regions in vacuolar membranes, are sites of membrane invagination during LD uptake. The endosome sorting complex required for transport (ESCRT) is required for sterol transport during L_o formation under these conditions. However, ESCRT has been implicated in mediating membrane invagination during μLP induced by ER stressors or the diauxic shift from glycolysis- to respiration-driven growth. Here we report that ER stress induced by lipid imbalance and other stressors induces L_o microdomain formation. This process is ESCRT independent and dependent on Niemann-Pick type C sterol transfer proteins. Inhibition of ESCRT or L_o microdomain formation partially inhibits lipid imbalance-induced μLP, while inhibition of both blocks this μLP. Finally, although the ER stressors dithiothreitol or tunicamycin induce L_o microdomains, μLP in response to these stressors is ESCRT dependent and L_o microdomain independent. Our findings reveal that L_o microdomain formation is a yeast stress response, and stress-induced L_o microdomain formation occurs by stressor-specific mechanisms. Moreover, ESCRT and L_o microdomains play functionally distinct roles in LD uptake during stress-induced μLP.**

Monitoring Editor
Sharon Tooze
The Francis Crick Institute

Received: Apr 14, 2021
Revised: Sep 30, 2021
Accepted: Oct 5, 2021

INTRODUCTION

Lipid droplets (LDs), organelles that form at and bud from ER membranes, consist of a phospholipid monolayer with associated proteins surrounding a core of neutral lipids including triacylglycerol and sterol esters. LDs have well-established functions in storage of lipids that are used for energy production or for synthesis of membrane components, signaling molecules, and other macromolecules. Storage of lipids within LDs also protects cells from exposure to excess free fatty acids or sterols (Kounakis *et al.*, 2019). Finally, recent studies revealed a role for LDs in protein quality control (Welte and Gould, 2017; Garcia *et al.*, 2018). Indeed, studies from our laboratory indicate that LDs function in removing unfolded proteins that accumulate in ER during ER stress and targeting those proteins for autophagic degradation by the lysosome (vacuole in yeast) (Vevea *et al.*, 2015; Garcia *et al.*, 2020). The central role of LD function in cellular fitness is evident from diseases such as obesity, nonalcohol fatty liver disease, cardiovascular disease, neutral lipid storage disease, lipodystrophy, and hereditary spastic paraplegia that are associated with LD dysregulation (Olzmann and Carvalho, 2019).

LDs are taken up into vacuoles for degradation by multiple autophagic pathways, referred to collectively as lipophagy. During macroautophagy-driven lipophagy, LDs are engulfed within autophagosomes, which fuse with and are degraded by lysosomes/vacuoles (Singh *et al.*, 2009). In contrast, during microautophagy-driven lipophagy (microlipophagy, μLP), LDs undergo

This article was published online ahead of print in MBoC in Press (http://www.molbiolcell.org/cgi/doi/10.1091/mbc.E21-04-0179) on October 20, 2021.

Competing interests: The authors declare no competing interests.

†P-CL and EJG contributed equally to these studies.

Author contributions: conceptualization: L.A.P., P.-C.L., and E.J.G.; methodology: P.-C.L. and E.J.G.; formal analysis: P.-C.L., E.J.G., and G.T.; investigation: P.-C.L., E.J.G., G.T., and C.A.T.; writing: L.A.P., P-C.L., and E.J.G.; supervision: L.A.P., P.-C.L., and E.J.G.; funding acquisition: L.A.P. and E.J.G.

*Address correspondence to: Liza A. Pon (lap5@cumc.columbia.edu).

Abbreviations used: DTT, dithiothreitol; ESCRT, endosome sorting complex required for transport; GR, glucose restriction; LD, liquid droplet; MVB, multivesicular body; NPC, Niemann-Pick type C; NVJ, nuclear–vacuolar junction; PC, phosphatidylcholine; PE, phosphatidylethanolamine; SC, synthetic complete; TCE, 2,2,2-trichloroethanol; TM, tunicamycin; UPR, unfolded protein response; YPD, yeast-peptone-dextrose; WT, wild type.

autophagosome-independent direct uptake into the lysosomes/vacuoles. In yeast, μLP is critical for mobilizing lipids for ATP production under nutrient-limited conditions, degrading excess lipids under conditions of lipid imbalance, degrading misfolded or aggregated proteins that are sequestered to LDs and targeting lipids and sterols to the vacuolar membranes (van Zutphen *et al.*, 2014; Wang *et al.*, 2014; Vevea *et al.*, 2015; Oku *et al.*, 2017; Seo *et al.*, 2017; Tsuji *et al.*, 2017; Garcia *et al.*, 2020). Recent studies revealed that μLP occurs in hepatocytes in response to nutrient limitation. As in yeast, hepatocyte μLP involves autophagosome-independent interaction of LDs with lysosomes and uptake of LDs into lysosomes at sites of invagination in the lysosomal membrane (Schulze *et al.*, 2020).

The mechanism of LD uptake into lysosomes in mammalian systems is not well understood. However, studies in yeast revealed two possible mechanisms for vacuolar membrane invagination during μLP. During transition into stationary phase or nitrogen starvation, LD uptake occurs at liquid-ordered (L_o) microdomains in the vacuolar membrane (Wang *et al.*, 2014; Tsuji *et al.*, 2017). L_o microdomains are specialized raftlike regions that are enriched in sterols and saturated lipids and specific proteins and coexist with liquid-disordered (L_d) domains. They are sites for membrane bending and invagination (Simons and Ikonen, 1997; Tsuji and Fujimoto, 2018).

L_o microdomains of the yeast vacuolar membrane are larger and more stable than other rafts (Toulmay and Prinz, 2013). Ultrastructural studies in yeast reveal that entry into stationary phase or nutrient limitation induces vacuolar L_o microdomain formation and roles for multivesicular bodies (MVBs, late endosomes that contain sterol-rich intraluminal vesicles) and Niemann-Pick type C (NPC) sterol transporter proteins, Ncr1 and Npc2, in this process. Specifically, MVBs mediate transport of sterols to the vacuole while NPC proteins transfer sterols from the lumen to membrane of vacuoles during L_o microdomain formation and expansion. These studies also find that L_o microdomains are a site for LD uptake into the vacuole during μLP, and that MVBs and NPC proteins are also required for this LD uptake (Tsuji *et al.*, 2017).

Studies from our laboratory and others revealed an alternative mechanism for LD uptake at the vacuole during μLP in yeast. This form of μLP depends on endosome sorting complex required for transport (ESCRT) and occurs in response to ER stressors or the diauxic shift from glycolysis- to respiration-driven growth (Vevea *et al.*, 2015; Oku *et al.*, 2017; Garcia *et al.*, 2020). Deletion of ESCRT components blocks μLP induced by these conditions. Moreover, ESCRT components are recruited to the vacuolar membrane and localize to sites of vacuolar membrane invagination and scission during LD uptake into the organelle (Vevea *et al.*, 2015; Oku *et al.*, 2017; Garcia *et al.*, 2020). These findings support the model that ESCRT plays a direct role in μLP in response to ER stressors or during the diauxic shift by mediating membrane invagination and scission during LD uptake into the vacuole. However, whether L_o microdomain-dependent and ESCRT-dependent mechanisms interact is still not clear.

Here we obtained additional evidence that L_o microdomain biogenesis is induced by multiple stressors in yeast and may be a general stress response. Moreover, we find that L_o microdomain formation occurs by different mechanisms in growing or stressed yeast compared with nutrient-limited yeast. Finally, our studies indicate that L_o microdomains and ESCRT have independent functions in LD uptake at the vacuolar membrane and that both mechanisms are active in μLP in yeast exposed to lipid imbalance.

RESULTS AND DISCUSSION

Lipid imbalance results in alteration of the redox state of ER

The ER houses key enzymes in all lipid biosynthetic pathways and is the site for trafficking and folding of 30% of the proteins in eukaryotic cells. Studies from our laboratory and others revealed that lipid imbalance, and more specifically, alterations in the ratio of phosphatidylcholine (PC) to phosphatidylethanolamine (PE), induces ER stress (Thibault *et al.*, 2012; Surma *et al.*, 2013; Vevea *et al.*, 2015). Since PC is a cylindrical lipid that stabilizes lipid bilayers and PE is a conical, bilayer-destabilizing lipid, PC:PE imbalance can induce ER stress through effects on lipid bilayer stress (Cullis *et al.*, 1996). On the other hand, we found that similar proteins are removed from the ER by LDs and targeted for degradation in response to lipid imbalance and treatment with dithiothreitol (DTT), a reducing agent that induces ER stress (Garcia *et al.*, 2020). This finding raises the possibility that lipid imbalance may also induce ER stress through effects on oxidative protein folding in the ER. We tested this hypothesis using an ER-targeted, redox-sensing GFP (eroGFP) (Merksamer *et al.*, 2008).

Here, lipid imbalance was induced using a model system described previously (Vevea *et al.*, 2015). *CHO2* encodes a phosphatidyl methyltransferase that catalyzes the first step in the conversion of PE to PC during de novo PC biosynthesis. In *cho2*Δ cells, PC can also be produced from exogenous choline (*cho2*Δ^{+C1}). However, withdrawal of choline from the medium for 1 d (*cho2*Δ^{-C1}) results in defects in PC biosynthesis, severe imbalance in the PC:PE ratio, and activation of the unfolded protein response (UPR), LD biogenesis and μLP (Vevea *et al.*, 2015).

We confirmed that the ER lumen is an oxidizing environment. Indeed, treatment with the oxidizing agent H_2O_2 did not cause a detectable change in the redox state of the ER lumen using the eroGFP indicator (Figure 1, A and B). In contrast, the ER lumen became 3.6-fold more reduced on treatment with DTT. We also found that lipid imbalance rendered the ER lumen 1.4-fold more reduced compared with that observed in nonstressed control cells (Figure 1). These findings support the model that the accumulation of unfolded proteins and UPR activation in response to lipid stress may be due in part to defects in oxidative folding in the ER.

Lipid imbalance and chemically induced ER stress induce vacuolar L_o microdomain formation

Our previous studies revealed that μLP is induced by all ER stressors studied (Vevea *et al.*, 2015; Garcia *et al.*, 2020); μLP in stationary-phase and nitrogen-starved yeast cells requires vacuolar L_o microdomains (Wang *et al.*, 2014; Tsuji *et al.*, 2017). However, whether a similar mechanism occurs during μLP in response to ER stress is still unknown. Here we tested the effect of ER stressors, including lipid imbalance, DTT, and tunicamycin (TM)-mediated inhibition of glycosylation of protein in the ER, on vacuolar L_o microdomains.

We confirmed that Vph1p and Ivy1p are effective for visualization of different types of L_o microdomains in yeast entering stationary phase (Martinez-Munoz and Kane, 2008; Dawaliby and Mayer, 2010; Toulmay and Prinz, 2013). Vph1p, a subunit of the vacuolar ATPase, localizes to vacuolar L_d domains and is excluded from L_o microdomains. In contrast, the phospholipid-binding inverse BAR protein Ivy1p localizes to punctate structures in L_o microdomains, where it mediates vacuolar membrane invagination during μLP (Toulmay and Prinz, 2013; Numrich *et al.*, 2015). Ivy1p also associates with components of the TORC1-regulating EGO complex and itself regulates the TORC1 complex (Numrich *et al.*, 2015). Since Ivy1p has functions that may be L_o independent, we scored L_o microdomains as sites in the vacuolar membrane where Vph1p is excluded and Ivy1p is enriched.

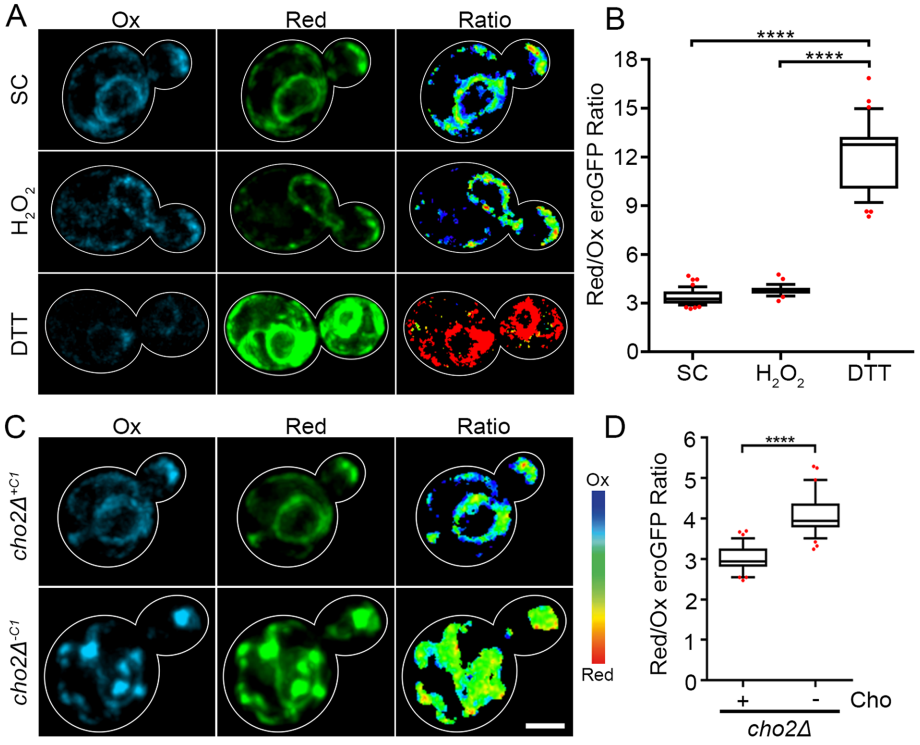

FIGURE 1: Lipid imbalance results in alteration of the redox state of ER. (A) Representative images of redox state of ER, visualized with eroGFP, in WT cells grown in SC and treated for 30 min with 5 mM DTT or 5 mM H_2O_2. Reduced, oxidized, and reduced:oxidized eroGFP ratio images are shown. Color scale in the bottom panel shows the dynamic range of ratios, with warmer colors indicating a more reducing environment. Bar, 2 µm. (B) Quantification of reduced:oxidized eroGFP ratios as shown in A. The box indicates the middle quartiles with the horizontal representing the median; whiskers show the 10th and 90th percentile, and red dots represent values in the top and bottom 10th percentiles. Representative trial from three independent experiments (n = 29–49 for each condition, ****$p < 0.0001$, by one-way ANOVA with Bonferroni's post-hoc test for multiple comparisons). (C) Representative images of redox state of ER in *cho2*Δ^{+C1} (normal lipid levels) and *cho2*Δ^{-C1} (lipid-stressed) cells visualized with eroGFP. Bar, 2 µm. (D) Quantification of reduced to oxidized eroGFP ratios in *cho2*Δ^{+C1} and *cho2*Δ^{-C1} cells as shown in C. Representative trial from three independent experiments (n = 35–38 for each condition, ****$p < 0.0001$, by unpaired two-tailed Student's t test).

L_o microdomains are classified into three groups defined by the shape and size of areas where Vph1 is excluded: type I L_o microdomains constitute large regions in the vacuolar membrane where Vph1p is excluded, type II L_o microdomains contain multiple smaller semisymmetrical Vph1p-free structures, and type III L_o microdomains contain small circular Vph1p-free regions that are similar in diameter and regularly spaced within the vacuolar membrane (Supplemental Figure S1A). Ivy1p localizes to all of these microdomains (Supplemental Figure S1B). As expected, all three types of L_o microdomains were evident in all cells within 1 to 2 d after entry into stationary phase and type II and III L_o microdomains in ~60% of cells during entry into stationary phase (Supplemental Figure S1, C and D). We also confirmed a significant increase in the number of Ivy1p puncta in yeast 2 d after entry into stationary phase (Supplemental Figure S1E) (Toulmay and Prinz, 2013; Wang *et al.*, 2014).

Next, we tested whether L_o microdomains form in midlog phase yeast that are exposed to lipid imbalance-, DTT-, or TM-induced ER stress. We detected regions in the vacuolar membrane that were Vph1p-free in some midlog phase cells (type I L_o microdomains). These regions are possible sites of contact of vacuoles with organelles including nuclei (at nuclear–vacuolar junctions, NVJs) and mitochondria (at vCLAMPs) (Kane, 2006; Martinez-Munoz and Kane, 2008; Dawaliby and Mayer, 2010; Takatori *et al.*, 2016). Using Vph1p exclusion as a marker, we detected an increase in the formation of type I and II L_o microdomains in yeast exposed to lipid imbalance- or DTT-induced ER stress (Figure 2, A, B, D, and E). However, L_o microdomain formation occurred to a lesser extent in ER-stressed yeast compared with that observed during entry into stationary phase (Figure 2, B and E, and Supplemental Figure S1D). Quantification of Vph1p exclusion in TM-treated yeast is difficult because vacuoles are highly fragmented, and the vacuolar membrane is not well resolved at sites of contact or overlap of fragmented vacuoles. Nonetheless, we observed a mild but insignificant increase in type I L_o microdomains in response to TM-induced ER stress (Supplemental Figure S1, F and G). We also detected a statistically significant increase in the number of Ivy1p puncta in vacuoles on exposure to any of the 3 ER stressors (Figure 2, C and F, and Supplemental Figure S1H). Thus we obtained evidence that lipid imbalance- and chemically induced ER stress both stimulate L_o microdomain formation.

L_o microdomains were originally identified in yeast exposed to short-term glucose starvation or treatment with cycloheximide or weak acids (Toulmay and Prinz, 2013). Other studies reveal that nitrogen limitation or transition into stationary phase induces L_o microdomain formation (van Zutphen *et al.*, 2014; Wang *et al.*, 2014; Tsuji *et al.*, 2017). Interestingly, hypertonic stress induces L_o microdomain formation at contact sites between vacuoles and nuclei, ER, mitochondria, or other vacuoles (Takatori *et al.*, 2016). Our finding that lipid imbalance and other ER stressors can induce L_o microdomain formation in yeast (Figure 2) provides additional evidence that vacuolar L_o microdomain formation is a general stress response.

Interestingly, L_o microdomain formation in response to ER stress and during transition to stationary phase may occur by distinct mechanisms. We detected an increase in all types of L_o microdomains in yeast transitioning into stationary phase (Supplemental Figure S1, C and D). In contrast, ER stress induced type I and II L_o microdomains in vacuoles, but no obvious type III microdomains (Figure 2, A, B, D, and E). In addition, the level of vacuolar L_o microdomains observed in response to ER stress is lower than that observed in stationary phase cells. It is possible that different types of L_o microdomains in vacuoles reflect maturation of those structures. However, it is also possible that there are functionally distinct L_o microdomain populations, reflected in part by microdomain type. These models are not mutually exclusive.

Impact of NPC and ESCRT proteins on ER stress-induced vacuolar L_o microdomain formation

During nutrient limitation-induced L_o microdomain formation, sterols are transferred to the vacuolar lumen by fusion of particles including MVBs, AP-3 vesicles, autophagosomes, or LDs with

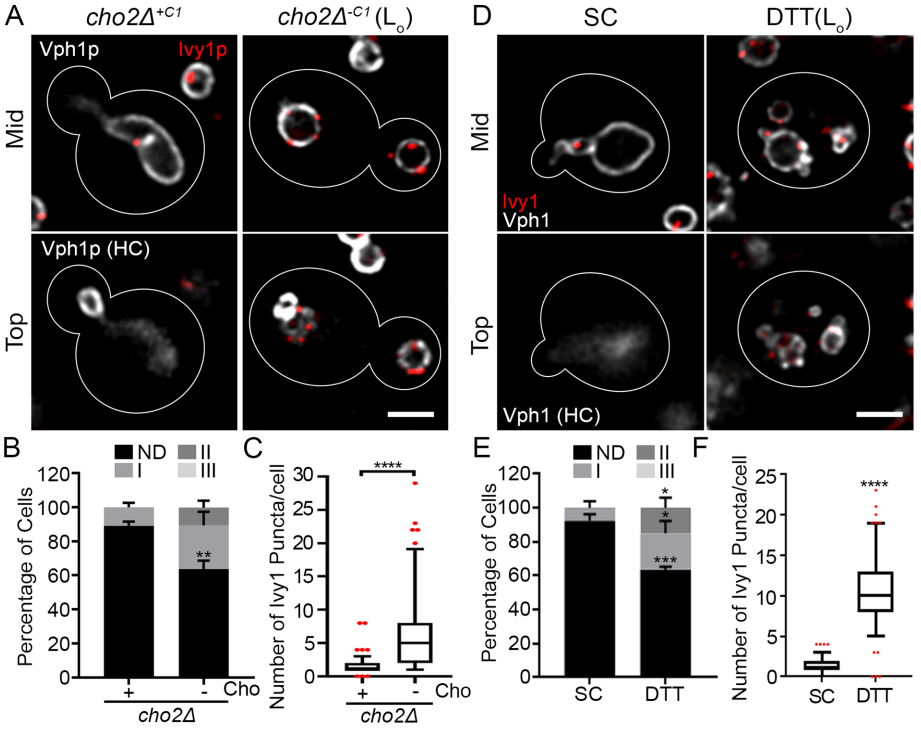

FIGURE 2: Lipid imbalance- and DTT-induced ER stress increase L_o microdomain formation. (A, D) Representative images of vacuoles with L_o domains in *cho2*Δ^{+C1}, *cho2*Δ^{-C1}cells (A), or WT cells grown in SC or SC + 5 mM DTT for 8 h (D). Cells express Ivy1p-GFPEnvy (red) and Vph1p-mCherry (gray). Mid, single optical section through the middle of the cell; Top, single optical section across the top of the vacuole; HC, high contrast. Bar, 2 µm. (B, E) Percentage of cells with vacuoles showing no L_o microdomains (ND) or L_o microdomain type I, II, or III in *cho2*Δ^{+C1} and *cho2*Δ^{-C1}cells (B); WT cells grown in SC or SC + 5 mM DTT for 8 h (E). Bars represent average + SEM from three independent trials ($n > 60$ cells for each condition per trial. *$p < 0.05$; **$p < 0.01$; ***$p < 0.001$, by unpaired two-tailed Student's *t* test). (C, F) Quantification of number of Ivy1p puncta per cell in *cho2*Δ^{+C1}, *cho2*Δ^{-C1}(C) and WT cells in SC or SC + 5 mM DTT for 8 h (F). Representative trial from three independent trials ($n > 40$ cells per conditions per trial. ****$p < 0.0001$ by unpaired two-tailed Mann–Whitney test).

vacuoles or by lipid transfer from other organelles at contact sites including NVJs or vCLAMPs (Tsuji and Fujimoto, 2018). Sterols within vacuoles are transferred to the vacuolar membrane for L_o microdomain formation by NPC proteins in stationary phase and nitrogen-limited yeast (Tsuji *et al.*, 2017). Here we studied whether NPC proteins and ESCRT, which mediates MVB formation, play roles in ER stress-induced L_o microdomain formation.

We found that deletion of *NCR1* and *NPC2* had no obvious effect on type I L_o microdomains in midlog phase yeast. In contrast, L_o microdomain formation in response to the ER stressors studied was partially inhibited by deletion of NPC proteins (Figure 3, A–D). Moreover, we detected a subtle reduction in type I L_o microdomains in TM-treated *ncr1*Δ *npc2*Δ yeast compared with wild-type (WT) yeast (Supplemental Figure S2, A and B). Finally, the increase in the number of Ivy1p puncta in vacuoles induced by all three ER stressors was also partially inhibited by deletion of NPC proteins (Supplemental Figure S2, C–E). Thus deletion of NPC proteins inhibits but does not block L_o microdomain formation in response to the ER stressors studied. This observation is consistent with previous findings that deletion of NPC proteins results in partial inhibition of L_o formation during transition into stationary phase or nitrogen starvation (Tsuji *et al.*, 2017).

We used fenpropimorph, an antifungal agent that inhibits enzymes in the ergosterol biosynthesis (Marcireau *et al.*, 1990), to assess the role of sterols in ER stress-induced L_o microdomain formation. We confirmed previous findings that fenpropimorph treatment effectively inhibits L_o microdomain formation in yeast during transition into stationary phase (Toulmay and Prinz, 2013). We also found that fenpropimorph compromised ER stress-induced L_o microdomain formation (Supplemental Figure S2, F and G). However, the inhibition of L_o microdomain formation observed during ER stress was subtle and less severe than that observed on entry into stationary phase or in *ncr1*Δ *npc2*Δ cells during ER stress or stationary phase. Thus, while sterol transfer is critical for L_o microdomain formation under all conditions studied, sterol biogenesis is a minor contributor to ER stress-induced L_o microdomain formation.

Next, we tested whether ESCRT is required for L_o microdomain formation in midlog phase cells and in cells exposed to ER stressors. We found that deletion of the ESCRT III component *SNF7* did not inhibit L_o microdomain formation in midlog phase yeast (Figure 4, A–D and Supplemental S3, A and B). Indeed, deletion of *SNF7* results in a subtle but statistically significant increase in exclusion of Vph1p at type I vacuolar L_o microdomains in midlog phase (Figure 4D and Supplemental Figure S3B). Moreover, deletion of *SNF7* or the ESCRT protein Vps4p did not affect L_o microdomain formation in cells challenged with DTT-, TM-, or lipid imbalance-induced ER stress (Figure 4, A–D and Supplemental Figure S3, A–D). Consistent with this, deletion of *VPS4* or *SNF7* had no effect on the localization of Npc2p to the vacuolar lumen or of Ncr1p to the vacuolar membrane under stress conditions (Figure 4, E–H and Supplemental Figure S3, E–H). Thus we found that ESCRT is not required for L_o microdomain formation in midlog phase cells or in yeast exposed to ER stressors.

Our studies revealed that mechanisms underlying L_o microdomain formation during stationary phase and midlog phase/ER stress are distinct. NPC proteins, presumably through their function in sterol transfer within the vacuole, are required for L_o microdomain formation in all cases. However, the source for sterols appears to be distinct during stationary phase compared with the other conditions studied. Previous studies indicate that ergosterol biosynthesis and ESCRT function in MVB-mediated transport of sterols to vacuoles are critical for L_o microdomain formation in stationary-phase yeast (Toulmay and Prinz, 2013; Tsuji *et al.*, 2017). In contrast, we find that inhibition of ergosterol biosynthesis has only minor effects and inhibition of ESCRT has no obvious effect on L_o microdomain formation in midlog phase or under ER stress. This finding is also supported by previous findings that treatment of vacuoles with methyl-β-cyclodextrin, an agent that extracts sterols from membranes, results in an increase in L_o microdomains in vacuoles in midlog phase yeast but reduces L_o microdomains in vacuoles in stationary-phase yeast (Toulmay and Prinz, 2013).

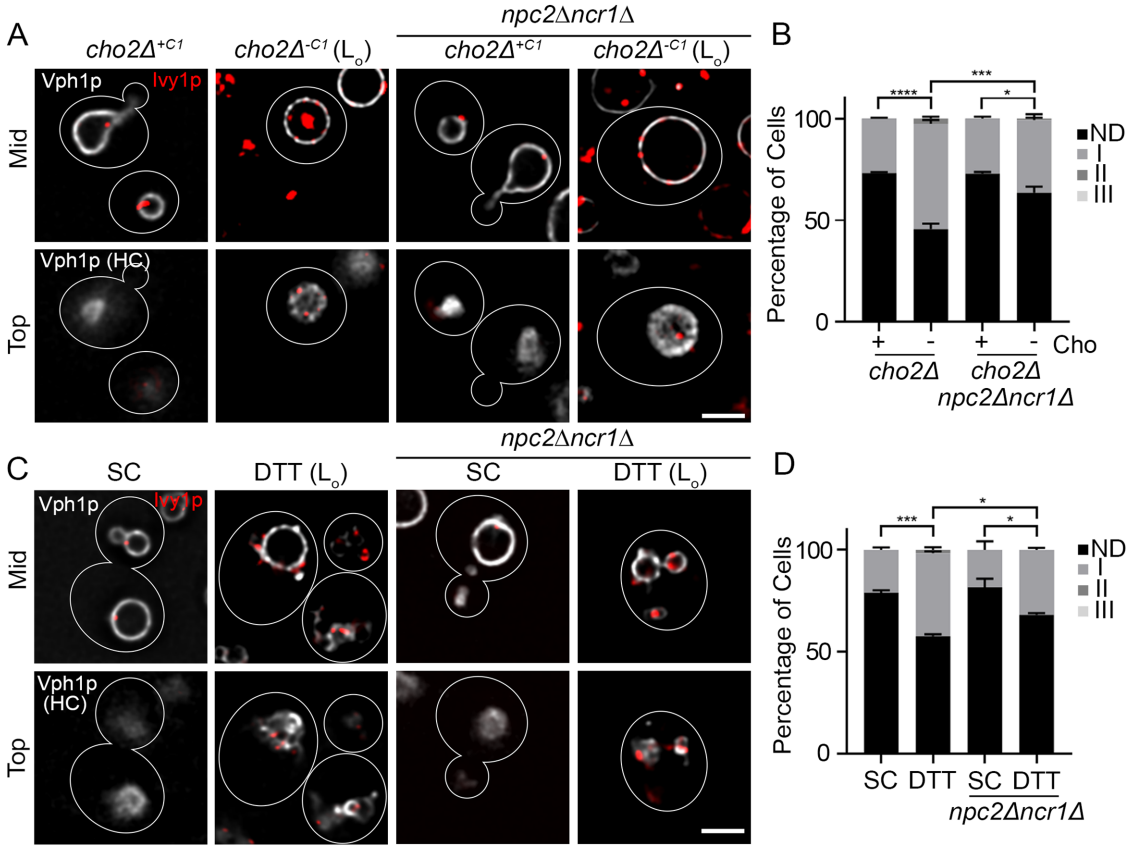

FIGURE 3: L_o microdomain formation under lipid imbalance- and DTT-induced ER stress is dependent on NPC proteins. (A, C) Representative images of vacuoles with L_o domains in *cho2*Δ^{+C1}, *cho2*Δ^{-C1}cells in the presence or absence of *NPC2* and *NCR1* (A), or WT cells in the presence or absence of *NPC2* and *NCR1* grown in SC or SC + 5 mM DTT for 8 h (C). Cells express Ivy1p-GFPEnvy (red) and Vph1p-mCherry (gray). Mid, single optical section through the middle of the cell; Top, single optical section across the top of the vacuole; HC, high contrast. Bar, 2 µm. (B, D) Percentage of cells with vacuoles showing no L_o microdomains or L_o microdomain type I, II, or III as shown in A and C, respectively. Bars represent average + SEM from three independent trials ($n > 60$ cells for each condition per trial. *$p < 0.05$; ***$p < 0.001$; ****$p < 0.0001$, by one-way ANOVA with Sidak's multiple comparisons test).

Differential roles for L_o microdomains and ESCRT in stress-induced µLP

Finally, we studied the relative contribution of L_o microdomains and ESCRT in vacuolar uptake of LDs during µLP. We observed an increase in the percentage of cells containing LDs within vacuoles in response to lipid or ER stress, which provides additional support for the notion that lipid or ER stress induces lipophagy (Supplemental Figure S4, A–F). We also used an established Western blot-based assay to measure lipophagy (Klionsky *et al.*, 2012; Vevea *et al.*, 2015). We tagged the LD marker protein Erg6p at its chromosomal locus with mCherry and carried out quantitative analysis of the degradation of Erg6p-mCherry to free mCherry. Using this assay, we found that lipid imbalance-, DTT-, or TM-induced ER stress induces Erg6p degradation and that this process is dependent on vacuolar proteases and does not require *ATG* genes (e.g., Figure 5, A–D and Supplemental Figure S4, G and H) (Vevea *et al.*, 2015; Garcia *et al.*, 2020). Thus, Erg6p degradation under the conditions studied is a sound readout for µLP.

We found that deletion of NPC proteins had no detectable effect on DTT- or TM-induced Erg6p degradation. In contrast, inhibition of ESCRT (by deletion of *SNF7*) blocked DTT- or TM-induced Erg6p degradation (Figure 5, A and B and Supplemental Figure S4, G and H). Since L_o microdomain formation requires NPC proteins during ER stress, our findings indicate that µLP in response to DTT- or TM-induced ER stress is not dependent on L_o microdomains. Moreover, we find that L_o microdomain formation during ER stress does not require ESCRT (Figure 4, A–D and Supplemental Figure S3, A–D). Since ESCRT localizes to sites of vacuolar membrane invagination and scission during ER stress-induced µLP (Garcia *et al.*, 2020), our findings support the model that ESCRT functions in DTT- or TM-induced µLP through effects on vacuolar membrane invagination and not through effects on L_o microdomain formation. Finally, we detected a statistically significant decrease in lipid imbalance-induced µLP in *ncr1*Δ *npc2*Δ cells (Figure 5, C and D) or in *snf7*Δ cells and a complete block in this process in *snf7*Δ *ncr1*Δ *npc2*Δ cells (Figure 5, C and D). These data support the model that vacuolar membrane invagination during µLP occurs by both L_o microdomain- and ESCRT-dependent mechanisms in response to lipid imbalance.

Overall, we find that ER stress induced by lipid imbalance and other stressors induces L_o microdomain formation, which is ESCRT independent and dependent on NPC proteins. Although all stressors can induce L_o microdomains, the contribution of L_o microdomains is different in response to different stressors. During DTT- or TM-induced ER stress, µLP is fully dependent on ESCRT and independent of NPC proteins. In contrast, LD uptake during lipid stress-induced µLP is both ESCRT and L_o microdomain dependent (Figure 5E). Our findings support the model that L_o microdomain formation

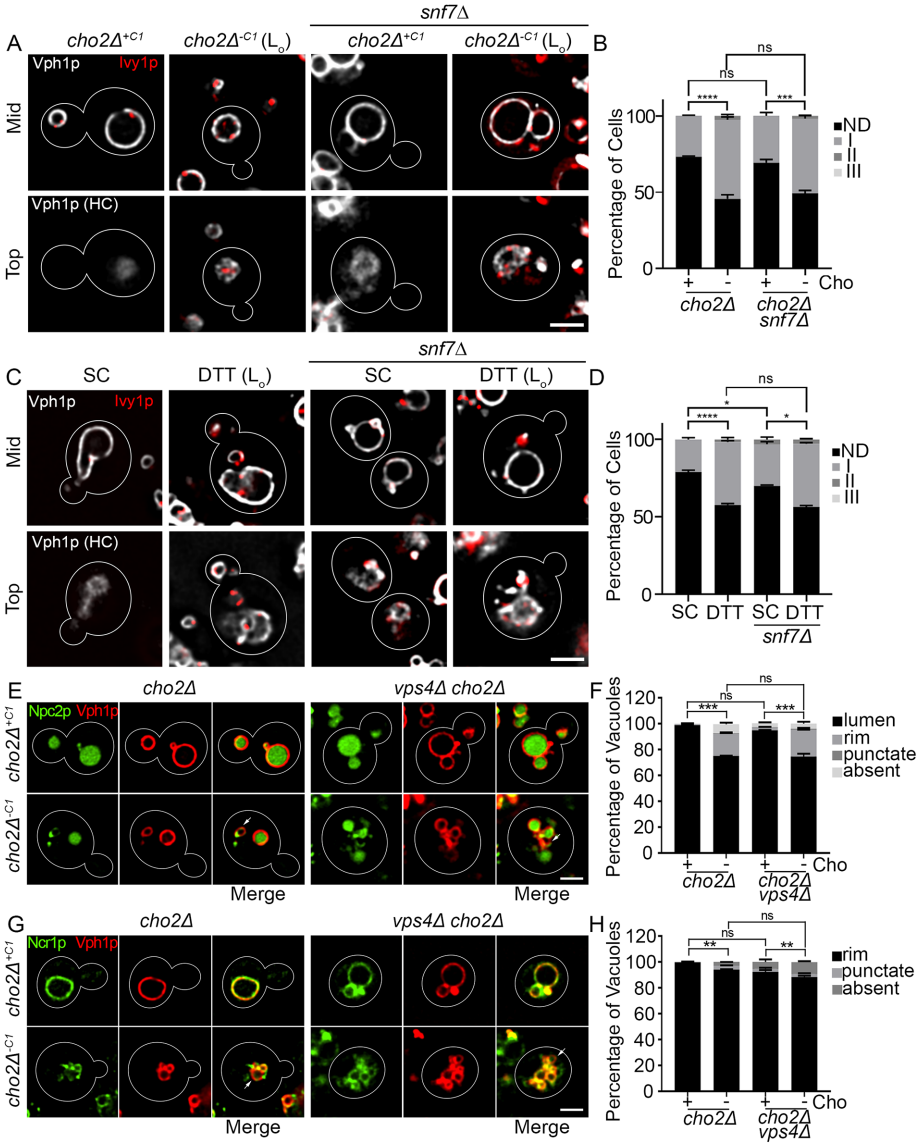

FIGURE 4: L_o microdomain formation under lipid imbalance- and DTT-induced ER stress is ESCRT-independent. (A, C) Representative images of vacuoles with L_o domains in *cho2*Δ^{+C1}, *cho2*Δ^{-C1}cells in the presence or absence of *SNF7* (A), or WT cells in the presence or absence of *SNF7* grown in SC or SC + 5 mM DTT for 8 h (C). Cells express Ivy1p-GFPEnvy (red) and Vph1p-mCherry (gray). Mid, single optical section through the middle of the cell; Top, single optical section across the top of the vacuole; HC, high contrast. Bar, 2 µm. (B, D) Percentage of cells with vacuoles showing no L_o microdomains (ND) or L_o microdomain type I, II, or III as shown in A and C, respectively. Bars represent average + SEM from three independent trials ($n > 60$ cells for each condition per trial. *$p < 0.05$; ***$p < 0.001$; ****$p < 0.0001$; ns, no significance; by unpaired one-way ANOVA with Sidak's multiple comparisons test). (E, G) Representative images of *cho2*Δ and *vps4*Δ*cho2*Δ cells tagged with Npc2p-GFPEnvy (E) or Ncr1p-GFPEnvy (G) and Vph1p-mCherry grown with (*cho2*Δ^{+C1}) or without (*cho2*Δ^{-C1}) 1 mM choline for 24 h. Images are single optical sections through the middle of the cell. Arrows show no lumen structures in (E) or no rim structures in (G). Bar, 2 µm. (F, H) Quantification of Npc2p (F) and Ncr1 (H) localization in vacuoles from images in (E) and (G), respectively. Graph shows average + SEM of the total percentage of vacuoles that show Npc2p (F) or Ncr1p (H) inside the vacuole (lumen), at the rim, in puncta, or absent from each vacuole. ($n = 3$, **$p < 0.01$; ***$p < 0.001$; ns, no significance by one-way ANOVA with Bonferroni's post-hoc test for multiple comparisons).

Previous studies raise the possibility that there are functionally distinct types of L_o microdomains. In midlog phase cells, Vph1p is excluded from regions in the vacuolar membrane (type I L_o microdomains) at NVJs and vCLAMPs (Kane, 2006; Martinez-Munoz and Kane, 2008; Dawaliby and Mayer, 2010; Takatori *et al.*, 2016). On the other hand, type III L_o microdomains are the primary sites for vacuolar membrane invagination during LD uptake in µLP induced by nutrient limitation (Tsuji *et al.*, 2017). We find that L_o microdomains contribute to lipid imbalance-induced LD uptake. Since type I and II L_o microdomains are the only microdomains that are detected under these conditions, our findings imply that LD uptake occurs at I or II L_o microdomains and provide additional support for the idea that the types of L_o microdomains are functionally distinct. Further studies may reveal the function of and markers for different populations of L_o microdomains.

It is not clear why LD uptake during µLP occurs under lipid imbalance-induced ER stress by two independent mechanisms but is entirely ESCRT dependent under DTT- or TM-induced ER stress. It is possible that lipid imbalance results in changes in the lipid composition of the vacuolar or LD membrane, which affect L_o microdomain formation or function, or LD interactions with vacuolar membranes. Alternatively, previous studies indicate that ESCRT function in lipophagy differs in cells exposed to acute glucose restriction (GR) compared with gradient, less severe GR (Zhang *et al.*, 2020). Since ER redox state is perturbed to a greater extent by DTT treatment compared with lipid imbalance (Figure 1), the differential effects of these two stressors on LD uptake at the vacuole may be due to differences in the severity or nature of ER stress. Finally, it is possible that L_o microdomains induced by chemically induced ER stress are functionally distinct from those produced by phospholipid imbalance.

It is also not clear why DTT- and TM-induced ER stress induces formation of L_o microdomains that either do not function in or are not required for µLP induced by those stressors. What, then, is the function(s) of L_o microdomains under these conditions? Do stress-induced L_o microdomains promote formation or stabilization of contact sites between vacuoles and other organelles, and if so, how do those contacts contribute to the cellular stress response? What is the mechanism for stress-induced L_o microdomain formation? Ongoing and future studies are needed to address these questions.

is a general stress response that occurs by distinct stressor-specific mechanisms. They also indicate that ESCRT and L_o microdomains play functionally distinct roles in LD uptake during stress-induced µLP.

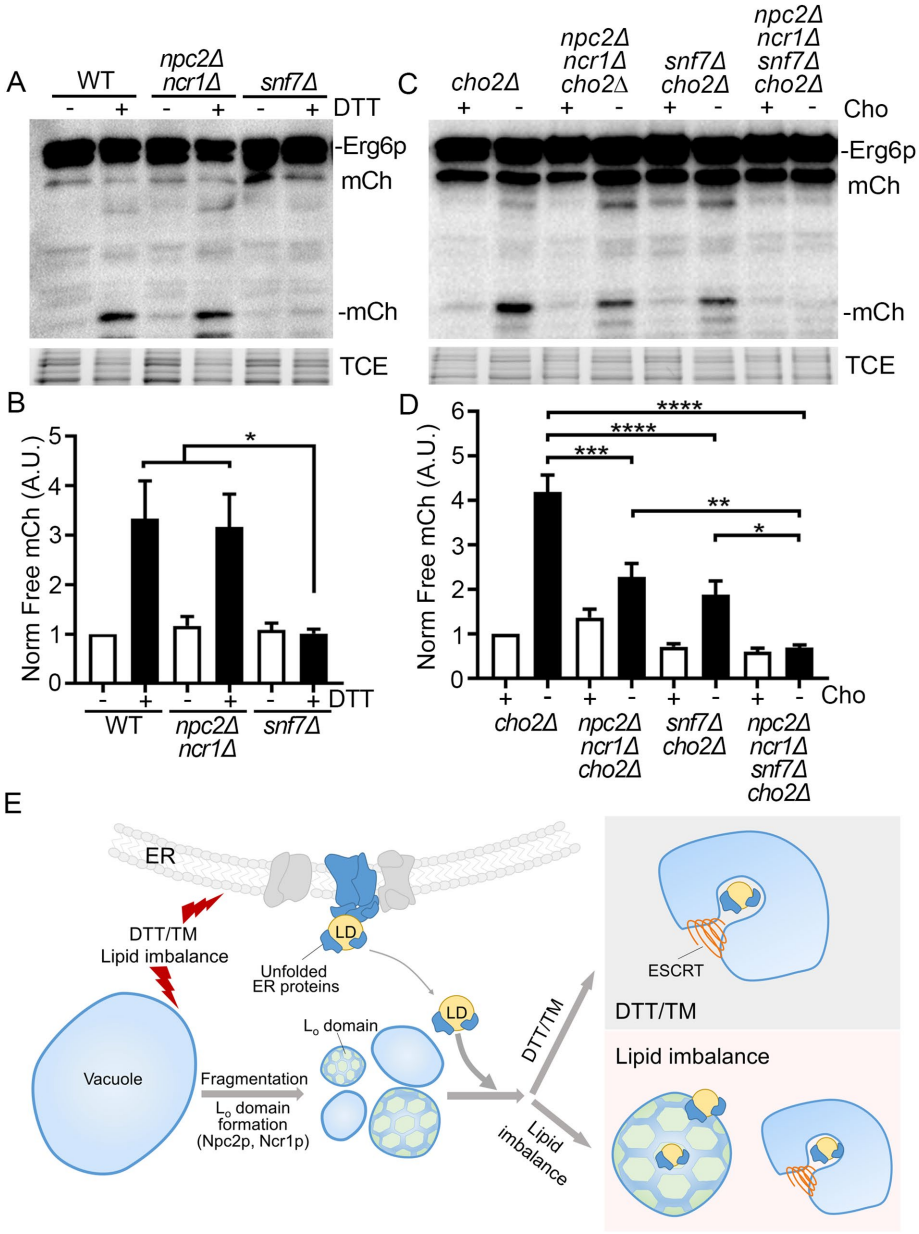

FIGURE 5: ESCRT and L_o microdomains have differential roles in μLP in response to lipid imbalance or DTT-induced ER stress. (A, C) Representative Western blots of Erg6p-mCherry in *cho2Δ*, *npc2Δncr1Δcho2Δ*, *snf7Δcho2Δ*, and *npc2Δncr1Δsnf7Δcho2Δ* cells grown with or without 1 mM choline (Cho) for 24 h (A), or in WT, *npc2Δncr1Δ*, and *snf7Δ* cells grown in SC, SC + 5 mM DTT for 8 h (C). (B, D) Quantification of vacuolar degradation of Erg6p-mCherry from Western blots in A and C. Bar graph shows average + SEM of total intensity of free mCherry bands normalized to TCE for each lane and to *cho2*Δ^{+C1}or WT. ($n = 15$ and $n = 9$ independent trials in F and H, respectively. *$p < 0.05$, **$p < 0.01$, ***$p < 0.001$, and ****$p < 0.0001$ by one-way ANOVA with Bonferroni's post-hoc test for multiple comparisons). (E) Schematic of the role of L_o microdomains and ESCRT in μLP under DTT-, TM-, or lipid imbalance-induced ER stress.

MATERIALS AND METHODS

Request a protocol through *Bio-protocol*.

Yeast strains and growth conditions

All strains were derived from WT BY4741 (*MATa his3Δ1 leu2Δ0 met15Δ0 ura3Δ0*) from Open Biosystems (GE Dharmacon, Lafayette, CO) and are listed in Table 1. All strains were grown at 30°C with shaking at 200 rpm (Sherman, 2002); *cho2Δ* yeast strains were grown on liquid rich-glucose medium (yeast-peptone-dextrose, YPD) or synthetic complete (SC) medium supplemented with 1 mM choline chloride (Sigma-Aldrich, St. Louis, MO) or on solid YPD supplemented with 4 mM choline chloride. To induce acute phospholipid imbalance, *cho2Δ* strains first were grown for 6 h on SC + 1 mM choline chloride until midlog phase (OD_{600} 0.10–0.35). Next, *cho2Δ* cells were washed once with choline-free SC medium and grown for 24 h on choline-free SC to induce acute phospholipid imbalance or on SC + 1 mM choline chloride to maintain normal phospholipid levels. Cells grown on SC + choline are noted as *cho2*Δ^{+C1}while cells undergoing acute phospholipid imbalance are noted as *cho2*Δ^{-C1} (Vevea *et al.*, 2015). Midlog phase cells were used in all experiments unless otherwise noted.

ER stress was induced by treating midlog phase cells for 8 h with 5 mM DL-DTT (Sigma-Aldrich, St. Louis, MO) or 2 μg/ml TM (Sigma-Aldrich, St. Louis, MO). Specifically, cells were grown overnight on SC to reach midlog phase. The following morning, cells were diluted and grown for 8 h on SC, SC + 5 mM DTT, or SC + 2 μg/ml TM until midlog phase unless otherwise noted. To reduce sterols, cells were treated with 5 μM fenpropimorph (Santa Cruz, Dallas, TX). For analysis at 2-d (2D) stationary phase, cells were grown as previously described (Wang *et al.*, 2014). Briefly, cells were grown overnight on SC to late midlog phase. The next day, cells were diluted to $OD_{600} = 0.15$ and allowed to continue growing. When the OD_{600} reached ~1.7, cells were left to grow for another 48 h before performing imaging experiments.

Yeast strain construction

To delete genes of interest, the loci of interest were replaced with an auxotrophy selection marker amplified from pOM12/13 (P30387/P30388 Euroscarf) or a *kanMX6* cassette from pFA6a-kanMX6 (Longtine *et al.*, 1998; Gauss *et al.*, 2005). pFA6a-kanMX6 was a gift from Jurg Bahler and John Pringle (Addgene plasmid #39296; RRID: Addgene_39296). These knockout strains were generated in corresponding amino acid dropout SC media or on YPD media with the required antibiotics (200 μg/ml G418 and 300 μg/ml hygromycin B; Sigma-Aldrich, St. Louis, MO) for selection.

To generate GFPEnvy or mCherry fusion proteins, GFPEnvy or mCherry was inserted in the endogenous locus at the C terminus of the coding sequence using modules amplified from pFA6a-link-GFPEnvy-SpHis5 (Slubowski *et al.*, 2015) or pCY3090-02 (Young *et al.*, 2012), respectively. pFA6a-link-GFPEnvy-SpHis5 was a gift from Linda Huang (Addgene plasmid # 60782; RRID:

Strain	Genotype	Source
BY4741	*MATahis3Δ1 leu2Δ0 met15Δ0 ura3Δ0*	Open Biosystems (Huntsville, AL)
EGS065	*MATahis3Δ1 leu2Δ0 met15Δ0 ura3Δ0 [pPM28-eroGFP:URA3]*	This study
EGS091	*MATahis3Δ1 leu2Δ0 met15Δ0 ura3Δ0 cho2Δ::LEU2 [pPM28-eroGFP:URA3]*	This study
EGS163	*MATahis3Δ1 leu2Δ0 met15Δ0 ura3Δ0 ERG6-mCherry::hphMX4*	This study
EGS203	*MATahis3Δ1 leu2Δ0 met15Δ0 ura3Δ0 ERG6-mCherry::hphMX4 snf7Δ::LEU2*	This study
EGS208	*MATahis3Δ1 leu2Δ0 met15Δ0 ura3Δ0 ERG6-mcherry::hphMX4 cho2Δ::LEU2*	This study
EGS222	*MATahis3Δ1 leu2Δ0 met15Δ0 ura3Δ0 ERG6-mCherry::hphMX4 VPH1-GFPEnvy::HIS3*	This study
EGS230	*MATahis3Δ1 leu2Δ0 met15Δ0 ura3Δ0 ERG6-mCherry::hphMX4 cho2Δ::LEU2 vps4Δ::KamMX6*	This study
EGS237	*MATahis3Δ1 leu2Δ0 met15Δ0 ura3Δ0 ERG6-mCherry::hphMX4 VPH1-GFPEnvy::HIS3 cho2Δ::LEU2*	This study
EGS270	*MATahis3Δ1 leu2Δ0 met15Δ0 ura3Δ0 NCR1-GFPEnvy::HIS3 VPH1-mCherry::hphMX4 cho2Δ::LEU2*	This study
EGS271	*MATahis3Δ1 leu2Δ0 met15Δ0 ura3Δ0 NPC2-GFPEnvy::HIS3 VPH1-mCherry::hphMX4 cho2Δ::LEU2*	This study
EGS295	*MATahis3Δ1 leu2Δ0 met15Δ0 ura3Δ0 ERG6-mCherry::hphMX4 cho2Δ::LEU2 snf7Δ::KanMX6*	This study
EGS316	*MATahis3Δ1 leu2Δ0 met15Δ0 ura3Δ0 NPC2-GFPEnvy::HIS3 VPH1-mCherry::hphMX4 cho2Δ::LEU2 vps4Δ::KanMX6*	This study
EGS317	*MATahis3Δ1 leu2Δ0 met15Δ0 ura3Δ0 VPH1-mCherry::hphMX4 IVY1-GFPEnvy::HIS3*	This study
EGS353	*MATahis3Δ1 leu2Δ0 met15Δ0 ura3Δ0 VPH1-mcherry::hphMX4 IVY1-GFPEnvy::HIS3 cho2Δ::LEU2*	This study
EGS377	*MATahis3Δ1 leu2Δ0 met15Δ0 ura3Δ0 ERG6-mCherry::hphMX4 npc2Δ::loxP ncr1Δ::URA3*	This study
EGS389	*MATahis3Δ1 leu2Δ0 met15Δ0 ura3Δ0 ERG6-mCherry::hphMX4 cho2Δ::LEU2 snf7Δ::URA3*	This study
EGS405	*MATahis3Δ1 leu2Δ0 met15Δ0 ura3Δ0 ERG6-mCherry::hphMX4 npc2Δ::loxP ncr1Δ::URA3 cho2Δ:: KamMX6*	This study
EGS458	*MATahis3Δ1 leu2Δ0 met15Δ0 ura3Δ0 ncr1Δ::URA3 npc2Δ::loxP snf7Δ::LEU2 cho2Δ:: KanMX6 ERG6-mCherry::hphMX4*	This study
EGS515	*MATahis3Δ1 leu2Δ0 met15Δ0 ura3Δ0 NCR1-GFPEnvy::HIS3 VPH1-mCherry::hphMX4 cho2Δ::LEU2 vps4Δ::KanMX6*	This study
CTY174	*MATahis3Δ1 leu2Δ0 met15Δ0 ura3Δ0 VPH1-mCherry-hphMX4 IVY1-ENVY-HIS3 snf7Δ::KanMX6*	This study
CTY175	*MATahis3Δ1 leu2Δ0 met15Δ0 ura3Δ0 VPH1-mCherry-hphMX4 IVY1-ENVY-HIS3 cho2Δ::LEU2 snf7Δ::KanMX6*	This study
CTY178	*MATahis3Δ1 leu2Δ0 met15Δ0 ura3Δ0 VPH1-mCherry-hphMX4 IVY1-ENVY-HIS3 npc2Δ::ura3 ncr1Δ::KanMX6*	This study
CTY179	*MATahis3Δ1 leu2Δ0 met15Δ0 ura3Δ0 VPH1-mCherry-hphMX4 IVY1-ENVY-HIS3 npc2Δ::ura3 ncr1Δ::KanMX6 cho2Δ::LEU2*	This study
CTY222	*MATahis3Δ1 leu2Δ0 met15Δ0 ura3Δ0 NCR1-GFPEnvy::HIS3 VPH1-mCherry::hphMX4 cho2Δ::LEU2 snf7Δ::KanMX6*	This study
CTY225	*MATahis3Δ1 leu2Δ0 met15Δ0 ura3Δ0 NPC2-GFPEnvy::HIS3 VPH1-mCherry::hphMX4 cho2Δ::LEU2 snf7Δ::KanMX6*	This study

TABLE 1: Yeast strains in this study.

Addgene_60782) while pCY 3090-02 was a gift from Anne Robinson (Addgene plasmid # 36231; RRID: Addgene_36231).

eroGFP strains were generated by transforming either WT or *cho2Δ* with pPM28 (eroGFP CEN/ARS URA3), a plasmid that expresses roGFP2-HDEL C-terminally fused to the signal sequence of Kar2p (Merksamer *et al.*, 2008). pPM28 was a gift from Feroz Papa (Addgene plasmid # 20131; RRID: Addgene_20131).

Analysis of ER redox potential

Strains transformed with pPM28 undergoing acute lipid imbalance or ER stress were imaged with an AxioObserver.Z1 microscope equipped with a 100×/1.3 oil EC Plan-Neofluar objective (Zeiss, Thornwood, NY) and an Orca-ER cooled CCD camera (Hamamatsu, Bridgewater, NJ) controlled by Zen Blue Edition (Zeiss). For validation of the probe, WT cells transformed with pPM28 were treated with 5 mM DTT or 5 mM H_2O_2 for 30 min and imaged. Oxidized and reduced channels were excited using a 405-nm LED and a 470-nm LED, respectively. Emission was acquired with a modified GFP filter (Zeiss filter 46 HE without excitation filter, dichroic FT 515, emission 535/30). Z-series were acquired through the entire cell with a z step of 0.3 μm and 1 × 1 binning. Images were deconvolved using a constrained iterative restoration algorithm assuming 507 nm excitation wavelength, 100% confidence level, and 60 iterations using Volocity 6.3 (Quorum Technologies, Puslinch, Ontario, Canada). The reduced:oxidized ratio channel was calculated by dividing the intensity of the reduced channel (λ_{ex} = 470 nm, λ_{em} = 525 nm) by the

intensity of the oxidized channel (λ_{ex} = 405 nm, λ_{em} = 525 nm) after background subtraction and thresholding for each channel individually.

Western Blotting

Western blot analysis was performed as previously described (Vevea *et al.*, 2015). Briefly, the same amount (0.5 OD_{600} • ml) of cells was collected for each condition and resuspended in 150 µl of lysis buffer (50 mM imidazole, pH 7.4, 10 mM EDTA, 1% triton X-100, 2 mM phenylmethylsulfonyl fluoride, and protease inhibitor cocktail: pepstatin A, chymostatin, antipain, leupeptin, aprotinin, benzamidine, and phenanthroline). Samples were vortexed with 100 µl of glass beads for 5 min. After vortexing, 50 µl of 4× SDS sample buffer was added and samples were boiled at 100°C for 10 min; 35 µl of protein lysate was loaded for each condition onto a 10% SDS–PAGE gel with 0.5% 2,2,2-trichloroethanol (TCE, Sigma-Aldrich, St. Louis, MO). Before transferring, TCE was activated by exposing the gel to UV light (300 nm) for 2.5 min to detect total loading proteins as loading control (Ladner *et al.*, 2004). Proteins were transferred to a PVDF membrane (Immobilon-FL; EMD Millipore, Billerica, MA). After transfer, the PVDF membrane was rinsed with H_2O and dried for 1 h prior to blocking with 3% skim milk in TBST for 1 h. Primary antibodies used include mouse monoclonal anti-mCherry (Abcam, Cambridge, MA; #ab125096; 1/2000 dilution) and mouse monoclonal anti-GFP (Proteintech, Rosemont, IL; 66002-1-Ig, 1/1000 dilution). Western blots were imaged using Luminata Forte Western HRP substrate (EMD Millipore, Billerica, MA) and the Chemidoc MP imaging system (Bio-Rad, Hercules, CA).

Western blot images were analyzed with Image Lab v5.2.1 (Bio-Rad, Hercules, CA) as follows. First, individual free mCherry bands were selected and a rolling disk background subtraction was applied with disk size = 10.0 mm. Later, the complete lane for each corresponding sample in the TCE image was selected and was analyzed with a rolling disk background subtraction with disk size = 70.0 mm. Total integrated intensity of free mCherry band was normalized to the integrated intensity of total protein loading control for each corresponding lane. Finally, for each independent experiment, all the samples were normalized to their experimental control, either *cho2*Δ^{+C1} cells or cells grown on SC.

Fluorescence microscopy

Yeast cells were collected by centrifuging for 30 s at 3,800 × *g* at RT, and 1.6 µl of cells were placed on a glass slide and covered with a #1.5 coverslip. Images were acquired with an Axioskop 2 microscope equipped with a 100×/1.4 Plan-Apochromat objective (Zeiss) and an Orca-ER cooled CCD camera (Hamamatsu) and a pE-4000 LED illumination system (coolLED, Andover, UK) controlled by NIS Elements 4.60 Lambda software (Nikon, Melville, NY). GFP and mCherry were excited using a 470-nm LED with a ET470/40× filter and a 561-nm LED with a ET572/35× filter, respectively (Chroma, Bellows Falls, VT). Emission was collected through a dual eGFP/mCherry cube (59222, Chroma, Bellows Falls, VT). GFP and mCherry images were deconvolved using a constrained iterative restoration algorithm assuming 507 nm and 610 nm excitation wavelength, respectively, with 100% confidence limit and 60 iterations using Volocity 6.3.

All image analysis and processing were performed with Volocity 6.3 or Fiji (Schindelin *et al.*, 2012). For visualization, all images were contrast-enhanced with similar parameters in each channel. All the analysis was performed on deconvolved unenhanced images. To measure the colocalization levels, images were thresholded and colocalization between ER proteins and LDs was quantified by measuring Manders' overlap coefficient (R) for each cell in Volocity 6.3 (Dunn *et al.*, 2011). To measure integrated intensity, objects of interests (ROI) were first identified after thresholding and appropriate size exclusion on the deconvolved images. The total integrated intensity for each cell was determined by the sum of voxel values of all identified objects in the cell.

Statistical Analysis

GraphPad Prism7 (GraphPad Software) was used for statistical analysis. All data were analyzed for normality with the D'Agostino and Pearson normality test. For comparison of two groups, *p* values were determined with an unpaired two-tailed Student's *t* test for parametric distributions and an unpaired Mann–Whitney test for nonparametric data. For multiple group comparisons, *p* values were determined with a one-way ANOVA with a Bonferroni post-hoc test or a Sidak's multiple comparisons test for parametric distributions and a Kruskal–Wallis test with Dunn's post-hoc test for nonparametric distributions. Bar graphs show the mean and SEM, while boxes indicate the middle quartiles with the midline representing the median. For all tests, *p* values are classified as follows: $*p < 0.05$; $**p < 0.01$; $***p < 0.001$; $****p < 0.0001$.

ACKNOWLEDGMENTS

We thank members of the Pon laboratory for technical assistance and valuable discussion. This work was supported by awards from the National Institutes of Health (NIH) (GM45735, GM122589, and AG051047) to L.A.P. and the NIH (GM007367 and AR070013) to E.J.G. We thank Theresa Swayne in the Confocal and Specialized Microscopy Shared Resource (CSMSR) in the Herbert Irving Comprehensive Cancer Center at Columbia University Medical Center for valuable discussion. The CSMSR is supported in part by an award from the NIH/NCI (5 P30 CA13696).

REFERENCES

Cullis PR, Fenske DB, Hope MJ (1996). Chapter 1 - Physical properties and functional roles of lipids in membranes. In: New Comprehensive Biochemistry, Vol. 31, ed. D.E. Vance and J.E. Vance, New York: Elsevier, 1–33.

Dawaliby R, Mayer A (2010). Microautophagy of the nucleus coincides with a vacuolar diffusion barrier at nuclear-vacuolar junctions. Mol Biol Cell 21, 4173–4183.

Dunn KW, Kamocka MM, McDonald JH (2011). A practical guide to evaluating colocalization in biological microscopy. Am J Physiol Cell Physiol 300, C723–C742.

Garcia EJ, Liao PC, Tan G, Vevea JD, Sing CN, Tsang CA, McCaffery JM, Boldogh IR, Pon LA (2020). Membrane dynamics and protein targets of lipid droplet microautophagy during ER stress-induced proteostasis in the budding yeast, Saccharomyces cerevisiae. Autophagy 1–21. doi: 10.1080/15548627.2020.1826691.

Garcia EJ, Vevea JD, Pon LA (2018). Lipid droplet autophagy during energy mobilization, lipid homeostasis and protein quality control. Front Biosci (Landmark Ed) 23, 1552–1563.

Gauss R, Trautwein M, Sommer T, Spang A (2005). New modules for the repeated internal and N-terminal epitope tagging of genes in Saccharomyces cerevisiae. Yeast 22, 1–12.

Kane PM (2006). The where, when, and how of organelle acidification by the yeast vacuolar H+-ATPase. Microbiol Mol Biol Rev 70, 177–191.

Klionsky DJ, Abdalla FC, Abeliovich H, Abraham RT, Acevedo-Arozena A, Adeli K, Agholme L, Agnello M, Agostinis P, Aguirre-Ghiso JA, *et al.* (2012). Guidelines for the use and interpretation of assays for monitoring autophagy. Autophagy 8, 445–544.

Kounakis K, Chaniotakis M, Markaki M, Tavernarakis N (2019). Emerging Roles of Lipophagy in Health and Disease. Front Cell Dev Biol 7, 185.

Ladner CL, Yang J, Turner RJ, Edwards RA (2004). Visible fluorescent detection of proteins in polyacrylamide gels without staining. Anal Biochem 326, 13–20.

Longtine MS, McKenzie A 3rd, Demarini DJ, Shah NG, Wach A, Brachat A, Philippsen P, Pringle JR (1998). Additional modules for versatile and economical PCR-based gene deletion and modification in Saccharomyces cerevisiae. Yeast 14, 953–961.

Marcireau C, Guilloton M, Karst F (1990). In vivo effects of fenpropimorph on the yeast Saccharomyces cerevisiae and determination of the molecular basis of the antifungal property. Antimicrob Agents Chemother 34, 989–993.
Martinez-Munoz GA, Kane P (2008). Vacuolar and plasma membrane proton pumps collaborate to achieve cytosolic pH homeostasis in yeast. J Biol Chem 283, 20309–20319.
Merksamer PI, Trusina A, Papa FR (2008). Real-time redox measurements during endoplasmic reticulum stress reveal interlinked protein folding functions. Cell 135, 933–947.
Numrich J, Peli-Gulli MP, Arlt H, Sardu A, Griffith J, Levine T, Engelbrecht-Vandre S, Reggiori F, De Virgilio C, Ungermann C (2015). The I-BAR protein Ivy1 is an effector of the Rab7 GTPase Ypt7 involved in vacuole membrane homeostasis. J Cell Sci 128, 2278–2292.
Oku M, Maeda Y, Kagohashi Y, Kondo T, Yamada M, Fujimoto T, Sakai Y (2017). Evidence for ESCRT- and clathrin-dependent microautophagy. J Cell Biol 216, 3263–3274.
Olzmann JA, Carvalho P (2019). Dynamics and functions of lipid droplets. Nat Rev Mol Cell Biol 20, 137–155.
Schindelin J, Arganda-Carreras I, Frise E, Kaynig V, Longair M, Pietzsch T, Preibisch S, Rueden C, Saalfeld S, Schmid B, *et al*. (2012). Fiji: an open-source platform for biological-image analysis. Nat Methods 9, 676–682.
Schulze RJ, Krueger EW, Weller SG, Johnson KM, Casey CA, Schott MB, McNiven MA (2020). Direct lysosome-based autophagy of lipid droplets in hepatocytes. Proc Natl Acad Sci USA 117, 32443–32452.
Seo AY, Lau PW, Feliciano D, Sengupta P, Gros MAL, Cinquin B, Larabell CA, Lippincott-Schwartz J (2017). AMPK and vacuole-associated Atg14p orchestrate mu-lipophagy for energy production and long-term survival under glucose starvation. Elife 6, e21690.
Sherman F (2002). Getting started with yeast. Methods Enzymol 350, 3–41.
Simons K, Ikonen E (1997). Functional rafts in cell membranes. Nature 387, 569–572.
Singh R, Kaushik S, Wang Y, Xiang Y, Novak I, Komatsu M, Tanaka K, Cuervo AM, Czaja MJ (2009). Autophagy regulates lipid metabolism. Nature 458, 1131–1135.
Slubowski CJ, Funk AD, Roesner JM, Paulissen SM, Huang LS (2015). Plasmids for C-terminal tagging in Saccharomyces cerevisiae that contain improved GFP proteins, Envy and Ivy. Yeast 32, 379–387.
Surma MA, Klose C, Peng D, Shales M, Mrejen C, Stefanko A, Braberg H, Gordon DE, Vorkel D, Ejsing CS, *et al*. (2013). A lipid E-MAP identifies Ubx2 as a critical regulator of lipid saturation and lipid bilayer stress. Mol Cell 51, 519–530.
Takatori S, Tatematsu T, Cheng J, Matsumoto J, Akano T, Fujimoto T (2016). Phosphatidylinositol 3,5-Bisphosphate-Rich Membrane Domains in Endosomes and Lysosomes. Traffic 17, 154–167.
Thibault G, Shui G, Kim W, McAlister GC, Ismail N, Gygi SP, Wenk MR, Ng DT (2012). The membrane stress response buffers lethal effects of lipid disequilibrium by reprogramming the protein homeostasis network. Mol Cell 48, 16–27.
Toulmay A, Prinz WA (2013). Direct imaging reveals stable, micrometer-scale lipid domains that segregate proteins in live cells. J Cell Biol 202, 35–44.
Tsuji T, Fujimoto M, Tatematsu T, Cheng J, Orii M, Takatori S, Fujimoto T (2017). Niemann-Pick type C proteins promote microautophagy by expanding raftlike membrane domains in the yeast vacuole. Elife 6.
Tsuji T, Fujimoto T (2018). Lipids and lipid domains of the yeast vacuole. Biochem Soc Trans 46, 1047–1054.
van Zutphen T, Todde V, de Boer R, Kreim M, Hofbauer HF, Wolinski H, Veenhuis M, van der Klei IJ, Kohlwein SD (2014). Lipid droplet autophagy in the yeast Saccharomyces cerevisiae. Mol Biol Cell 25, 290–301.
Vevea JD, Garcia EJ, Chan RB, Zhou B, Schultz M, Di Paolo G, McCaffery JM, Pon LA (2015). Role for lipid droplet biogenesis and microlipophagy in adaptation to lipid imbalance in yeast. Dev Cell 35, 584–599.
Wang CW, Miao YH, Chang YS (2014). A sterol-enriched vacuolar microdomain mediates stationary phase lipophagy in budding yeast. J Cell Biol 206, 357–366.
Welte MA, Gould AP (2017). Lipid droplet functions beyond energy storage. Biochim Biophys Acta 1862, 1260–1272.
Young CL, Raden DL, Caplan JL, Czymmek KJ, Robinson AS. (2012). Cassette series designed for live-cell imaging of proteins and high-resolution techniques in yeast. Yeast 29, 119–136.
Zhang A, Meng Y, Li Q, Liang Y (2020). The endosomal sorting complex required for transport complex negatively regulates Erg6 degradation under specific glucose restriction conditions. Traffic 21, 488–502.